Materials Chemistry and Physics 316 (2024) 129043

Contents lists available at ScienceDirect

Materials Chemistry and Physics

journal homepage: www.elsevier.com/locate/matchemphys

The investigation of synthesis and textured properties of in situ formed hBN with spark plasma sintering

Zuhal Yılmaz [a,*], Nuran Ay [b]

[a] Bilecik Şeyh Edebali University, SMYO, 11600, Bilecik, Turkey
[b] Eskişehir Technical University, Faculty of Engineering, Department of Materials Science and Engineering, 26555, Eskisehir, Turkey

HIGHLIGHTS

- With this method, hBN can be obtained with SPS.
- The highest orientation was obtained with an IOP value of −19925.5 at 1700 °C.
- This study, shows that highly oriented hBN textured ceramics can be synthesized in situ with SPS.
- The hBN can act as a barrier for heat conduction.

GRAPHICAL ABSTRACT

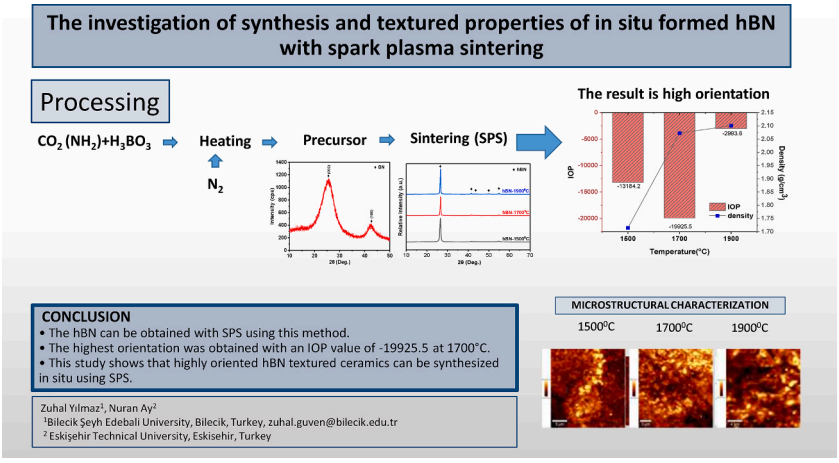

ARTICLE INFO

Keywords:
hBN
SPS
Textured properties
Thermal conductivity
Raman

ABSTRACT

Hexagonal boron nitride (hBN) exhibits high thermal conductivity within the in-plane direction and significantly lower thermal conductivity in the cross-plane direction because of its anisotropic nature. When the texture properties of bulk hBN are strong, it is a potentially promising application area for the insulating heat spreaders and heat sinks. In this study, hBN was synthesized in situ with the spark plasma sintering (SPS) technique and the effects of sintering temperature on the orientation of hBN grains were investigated. The precursor was prepared by chemically reacting urea and boric acid in heat treatment at 850 °C. The hBN was produced using the previous precursor in a SPS at 1500, 1700, and 1900 °C. The samples were characterized using XRD, FTIR, SEM and Raman spectroscopy. The properties of the samples were further determined through measurements of density, DSC and thermal diffusivity. The hBN samples obtained through the SPS process have nano and micron-size grains. The hBN was highly crystalline and homogeneous, as determined by the XRD pattern, Raman spectra and Raman maps. The orientation of hBN grains has been revealed in the c-axis of hBN crystallites and was preferably arranged within a plane parallel to the SPS pressing direction. The hBN orientation preference index

* Corresponding author. Bilecik Şeyh Edebali University, Söğüt Meslek Yüksekokulu, Ertuğrul Gazi Yerleşkesi, Türkmenbaşı, Mahallesi Bilecik Yolu 5, Sokak No:1, Söğüt/Bilecik, Turkey.
E-mail address: zuhal.guven@bilecik.edu.tr (Z. Yılmaz).

https://doi.org/10.1016/j.matchemphys.2024.129043
Received 24 November 2023; Received in revised form 22 January 2024; Accepted 9 February 2024
Available online 21 February 2024

(IOP) value of −19925.5 at 1700 °C indicates the highest quality texture orientation. Increasing the temperature to 1900 °C decreased the orientation in the direction parallel to the pressing direction. The highest thermal conductivity calculated according to the thermal diffusivity perpendicular to the sintering pressure direction was 8.86 W $m^{-1}K^{-1}$ at 1900 °C.

1. Introduction

Hexagonal boron nitride (hBN) is an inorganic material used in many industries because of its low elastic modulus, high thermal conductivity, high thermal shock resistance, electrical resistivity, low dielectric constant, chemical stability and excellent lubricity [1–4]. hBN is referred to as "white graphite" because its layered structure is very similar to graphite. Strong covalent bonding combined B and N atoms in the layer, while it has weak van der Waals interactions between the layers [3,5,6].

The first turbostratic boron nitride was synthesized by O'Connor by the reaction of boric acid (H_3BO_3) and urea ($CO(NH_2)_2$) [7–9]. Amorphous boron nitride (a-BN) is formed as a result of the reaction between boric acid and urea within a temperature range of 500–600 °C [9–11]. According to the literature, ammonium poly borates $(NH_4)_2B_4O_7$ are formed with the heat treatment of urea and boric acid at a range 250–300 °C, and ammonia is formed because of the reaction of a part of the urea with water. When the temperature rises to 500–600 °C, the ammonium poly borates react with ammonia to form a-BN according to the following equations [10];

$$4H_3BO_3 + CO(NH_2)_2 \rightarrow (NH_4)_2B_4O_7 + CO_2 + 4H_2O \quad (1)$$

$$CO(NH_2)_2 + H_2O \rightarrow 2NH_3 + CO_2 \quad (2)$$

$$(NH_4)_2B_4O_7 + NH_3 \rightarrow 4\ a\text{-}BN + 7H_2O \quad (3)$$

Turbostratic structure BN, an imperfect structure without three-dimensional order, is formed in the range of 900–1000 °C [12–15]. The content of the oxygen impurities was as high as 10% when calculated as boric oxide in this form [11]. The turbostratic structure crystallizes turns into a hexagonal form at temperatures above 1450–1500 °C [11,12,15].

The sinterability of hBN is very poor because of related to its structure. Therefore, pressure sintering techniques such as hot pressing (HP) and hot isostatic pressing (HIP) are often used with various sintering additions. These studies reported that the hBN grains are oriented perpendicular to the pressure axis during hot pressing, leading to anisotropic properties [3,5,16–21]. In prior studies, hBN was sintered using hot pressing and the effects of sintering pressures, temperature and various sintering additives on texture degrees, physical, mechanical and thermal conductivity properties were investigated. hBN sintering was carried out at different pressures and temperatures without sintering [17] and using Mullite [5,16], MAS (MgO powder, Al_2O_3 powder and fused silica powder) [18,19], metallic copper [3,20], Y_2O_3, Yb_2O_3, CaO, MgO (in different compositions) [21] and YAG (reaction between Y_2O_3 and Al_2O_3) [22,23] sintering additives. Textured hBN with preferentially oriented grain has anisotropic mechanical and thermal properties. This anisotropic thermal conductivity, together with its insulating property, makes hBN promising thermal management devices in electronics [23]. Therefore, developing these properties of hBN requires a thorough comprehension of its texture degrees properties.

SPS is a technique that sinters at low temperatures and for short periods of time by charging the gaps between powder particles with electrical energy. It effectively applies the high-temperature spark plasma formed in the first stage of energizing with an electromagnetic field and joule heating by the low-voltage continuous electric pulsed current. Compared to conventional sintering techniques such as pressureless sintering (PLS), HP and HIP, sintering can be performed at temperatures 200–300 °C lower and in short times such as 0–10 min [24–26]. SPS provides high heat efficiency by directly heating the powder material and graphite mold with a high pulsed current and homogeneous materials are produced because heating is uniform [24]. Therefore, SPS has been the focus of various studies because of its ability to produce products with superior properties compared to conventional methods.

There is increasing interest in the sintering of hBN using SPS [27–32]. In these studies in which sintering behavior, physical and mechanical properties were investigated, and already synthesized hBN was used. There is a study in which bulk BN with quasi-isotropic crystal structure and thermal conductivity was produced from boron nitride nanosheets (BNNSs) using the SPS technique and its texture properties were examined [27]. A study of hBN powder synthesis using SPS has also been reported in the literature, but sintering was not performed [33].

In this study, a precursor boron nitride powder was prepared using urea and boric acid, followed in-situ hBN production and sintering were performed together using SPS. The effects of sintering temperatures on texture degrees were investigated. Characterization of the samples was performed through XRD, FTIR, SEM, and Raman spectroscopy. The properties of the samples were determined with DSC, density and thermal diffusivity measurement.

2. Experimental procedure

The H_3BO_3 (Merck, Germany) and $CO(NH_2)_2$ (Merck, Germany, ≥ 99.5%) were used as starting raw materials. The molar ratio of (H_3BO_3): ($CO(NH_2)_2$) was 1:3 in powder. Starting raw materials were mixed on the heater/stirrer at a temperature of 80 °C with a 300 rpm cycle. The mixing was continued until the total evaporation of ethanol. Dried powder mixtures were transferred to an alumina combustion crucible and heated at two temperatures under a nitrogen atmosphere in a tube furnace (Protherm). It was first heated to 500 °C for 2 h and then heated to 850 °C for 12 h. Grinding of the obtained precursor powder was performed using an agate mortar. The powder was inserted directly into a graphite die with a diameter of 20 mm. The shaping and sintering were done in SPS (HPD-50, FCT GmbH, Germany) under 30 MPa pressure for 15 min at vacuum conditions for 1500 °C, 1700 °C and 1900 °C respectively. The electric current was pulsed periodically with 12 pulses/ms (2 of 12 pulses off as a recovery time). The production schematic diagram of the experimental procedure is given in Fig. 1. These samples were coded as hBN-1500, hBN-1700 and hBN-1900, with temperature.

The crystalline phases of the materials were determined using by X-Ray diffractometer (XRD- Rigaku Rint 2000). XRD patterns were obtained with Cu-Kα radiation (λ = 1.5418 Å), in the 2θ range of 10–70° with the scan speed of 2°/min at all samples. The XRD pattern after 850 °C heat treatment was obtained in the 2θ range of 10–50° with a scan speed of 1°/min. Infrared (IR) spectra of powder after heat treatment were recorded with a Fourier transform infrared spectrometer (Bruker Tensor 27) in the range of 700–4000 cm^{-1}. The chemical decomposition of powder after heat treatment was investigated by thermogravimetric analysis (Netzsch STA 449F3) up to 1400 °C under the nitrogen atmosphere. The sample's microstructure was characterized using scanning electron microscopy (SEM, ZEISS SUPRA 50 V P) and equipped with an energy-dispersive x-ray probe (EDS, Oxford Instruments, UK). The samples' Raman spectroscopic measurements and Raman mapping were performed on a Raman microscope (Konfokal WITec alpha300 R). Laser excitation of all samples is 532 nm for all Raman data with a laser power of 1.5 mW and the image mapping used 20 × 20 μm square areas with a laser power of 5 mW (1500 °C and 1900 °C) and 7 mW (1700 °C). The true density was measured with a Quantachrome Ultrafoam 1200e pycnometer using a 10 cm^3 sample

cup. The thermal diffusivity of samples was measured by using the Laser Flash spectrometer (NETZSCH LFA 457) at 25–400 °C range. Samples for diffusivity measurement were prepared in the size of 10 × 10 × 2 mm^3. Atomic force microscopy (AFM) images of the topography of the native material were obtained with the Gwyddion program from SEM images.

3. Results and discussion

3.1. Characterizations of precursor and sintered samples

The XRD patterns of the sample after heat treatment at 850 °C are shown in Fig. 2a. The figure showed that the heat treatment at 850 °C stared to form the turbostratic BN [34]. This structure has two diffraction peaks to the (002) and (100) reflection of hBN in the XRD pattern near 26° and near 43°, respectively, but still not possessing layers large enough to form perfectly crystalline material of hexagonal boron nitride [12]. The broadening of the peaks indicates the product has poor crystallization [35]. BN formation in the FTIR analysis shown in Fig. 2b is also supported by the hBN peaks. The FTIR spectrum has two characteristic peaks of hBN at 1368 and 796 cm^{-1} in the sample. The peak at 1368 cm^{-1} can be attributed to the B–N stretching vibrations of the sp^2-bonded hBN and the peak at 796 cm^{-1} is due to B–*N*–B bending vibrations [4,10]. According to the thermal analysis results after heat treatment at 850 °C, the reactions continue and mass change occurs in Fig. 2c. Mass losses appear at about ~13 % in the sample at up to 200 °C. The mass losses are caused by the removal of the OH- and H+ ions from the system with temperature. This is caused by the unreacted precursor because the urea and boric acid reactions are not completely fulfilled and the mass losses evaporation of the B_2O_3 at high temperatures. The reason for the mass increase in the range of 800–1000 °C is may be due to the nitrogen reacting during thermal analysis, which is responsible for contributing to the formation of BN and the growth of the plates [10,36].

SEM images of the material heat treated at 850 °C are shown in Fig. 3a. The formation of hBN plates is shown in this image. In the EDS analysis, there are boron, nitrogen and oxygen in this sample (Fig. 3b). The oxygen in EDS may result from the presence of residual boron oxides [9,15,36], as supported by the TG result. Hagio et al. [15] showed that the oxygen content from about half of which was as B_2O_3 from the raw materials decreased to only about half at 1000 °C. According to this study, the residual oxygen level decreased with increasing temperature, and when subjected to heat treatment above 1700 °C, the residual oxygen content was less than 1% by weight.

After SPS under pressure 30 MPa for 15 min at 1500 °C, 1700 °C and 1900 °C respectively, the XRD analysis performed on powdered samples (Fig. 4a) showed evidence that the crystalline structure agrees with the pattern for hBN (JCPDS PDF No: 034–0421). The temperature has significant importance on the grain size of the crystallite. The change in L_c crystallite size with increasing temperature was determined by calculating the width of the diffraction peak (002) of the XRD patterns in Fig. 4a According to Debye-Scherrer (Eq. (1)) [37,38]. The change in La crystallite size was calculated using the width of the diffraction peak (100) of the XRD patterns from the samples shown in Fig. 4a. The equation;

$$D = \frac{K\lambda}{\beta \cos\theta} \quad (1)$$

where D is the crystallite size, K is the shape factor (which is 0.941), λ is the wavelength of the X-rays (using Cu K(α) radiation source, 1.54060 Å), β is full width at half maximum (FWHM) of the peak and θ is the Bragg angle. The Debye-Scherrer L_c crystallite size of hBN was calculated to be 13.96 nm, 21.48 nm and 23.82 nm for hBN-1500, hBN-1700 and hBN-1900 samples, respectively. L_a crystallite size was calculated as 17.96 nm, 23.40 nm and 25.74 nm for the same samples. Clearly, that the size increased with the temperature [39].

The Raman spectrum was used to determine the bonding states of hBN (Fig. 4b), and the typical Raman spectrum showed a strong peak at ~1367 cm^{-1}, originating from the E_{2g} vibrational mode of hBN [40–44]. Fig. 4b shows that the Raman vibration peak is 1367.5 cm^{-1}, 1367.1 cm^{-1} and 1367.1 cm^{-1} for hBN-1500, hBN-1700 and hBN-1900 samples, respectively. In addition, the corresponding FWHM values were 18.02 cm^{-1}, 15.43 cm^{-1} and 13.70 cm^{-1}, they became narrower with the increasing sintering temperature. The reason for the narrower E_{2g} peak can be attributed to the increase in the size of ordered BN layers [44]. The L_a crystallite size is calculated from the Raman spectrum FWHM using the following Nemanich model formula (Eq. 2) [45–47];

$$L_a = 1417/(\Gamma_{1/2} - 8.7) \quad (2)$$

Where L_a is the crystallite size and $\Gamma_{1/2}$ is FWHM of E_{2g} vibrational Raman peak of hBN. The crystallite size of hBN was calculated as 15.2 nm, 21.1 nm and 28.3 nm for hBN-1500, hBN-1700 and hBN-1900 samples, respectively. The results indicate the crystallite size and crystallinity of hBN improve significantly with increasing temperature, which is consistent with the XRD results [48]. Raman map of strong hBN peaks at ~1367 cm^{-1} is shown in Fig. 4c–e. The Raman mapping is used to identify a variety of information such as crystallinity, homogeneity, defect sites, and binding at the molecular level. Raman spectroscopy mapping analysis is generally used for the characterization of low-dimensional nanostructured materials, coatings, and thin films [49]. In this study, Raman mapping was used for bulk-produced hBN. The 20 × 20 μm area was mapped and analyzed to explain the overall quality of hBN. The intensity ratio maps of hBN show that for hBN-1500, hBN-1700 and hBN-1900, these values are in the range from 1024 (black) to 2805 (yellow), 1333 (black) to 2569 (yellow) and 916 (black) to 2520 (yellow), respectively. According to the Raman maps, hBN shows a uniform distribution [49]. The dark regions in the Raman map may be attributed to the possibility of multilayer hBN and an increased concentration of defects and multilayer structure [50,51]. A monolayer of hBN gives a very weak Raman E_{2g} band, while the intensity of the Raman peak increases proportionally with the increasing number of layers [52]. The high Raman peak intensity (Fig. 4b) supports multilayer hBN. The occurrence of black and yellow regions on the Raman maps results from many layering of hBN, which is produced with a thickness of 2 mm since Raman maps are obtained from these surfaces.

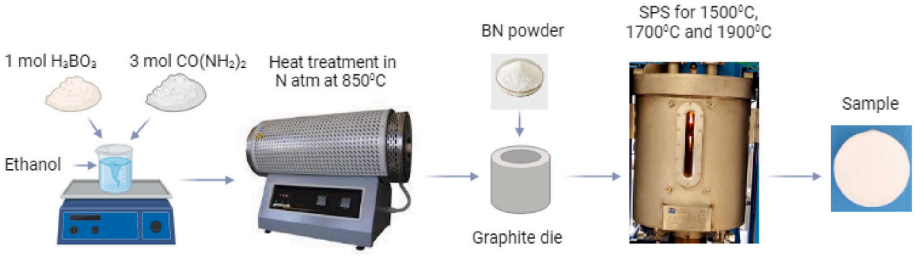

Fig. 1. The schematic diagram of production in the experimental procedure.

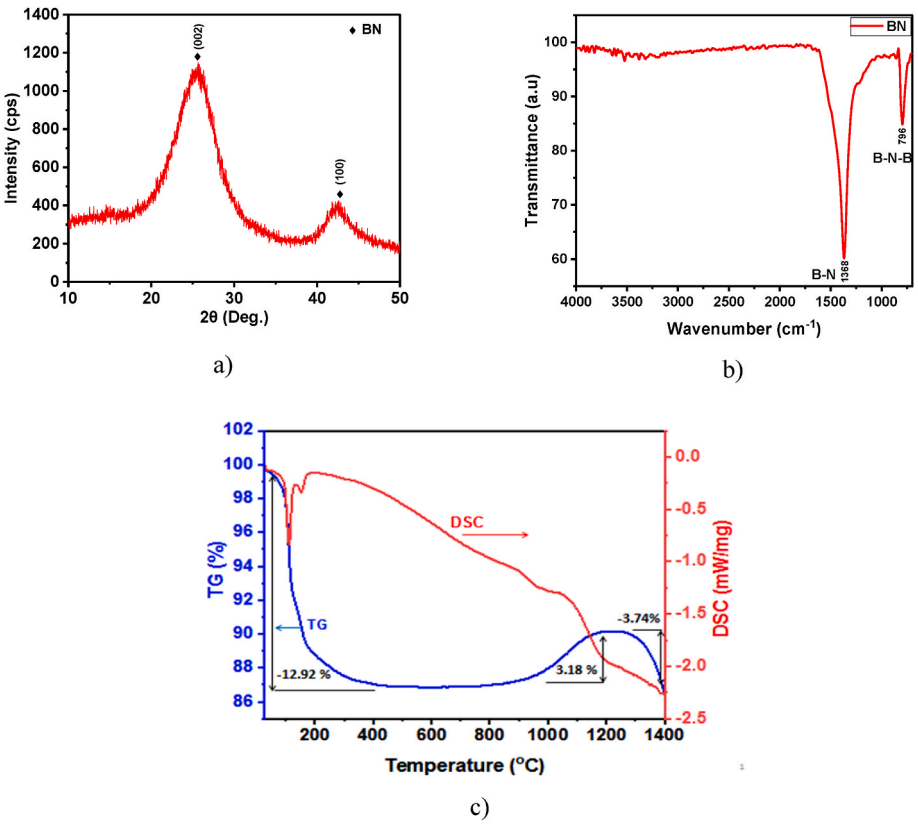

Fig. 2. After heat treatment of BN at 850 °C, a) XRD pattern, b) FTIR spectrum and c) TG-DSC curves at the N_2 atmosphere.

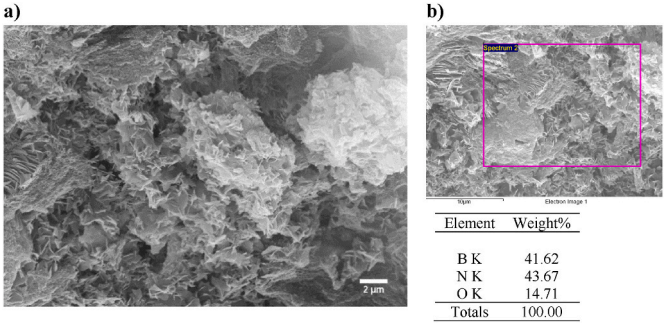

Element	Weight%
B K	41.62
N K	43.67
O K	14.71
Totals	100.00

Fig. 3. After heat treatment of BN at 850 °C a) SEM image b) EDS result.

3.2. Characterization of texture

A detailed understanding of texture degrees' properties of hBN is important for developing anisotropic properties. To determine the effects of the sintering temperature on the samples' orientation, orientation preference index (IOP) values were calculated from X-ray diffraction patterns. Samples were examined in two directions using the XRD pattern as displayed in Fig. 5. XRD patterns are shown on the top surface (TS) perpendicular to the sintering pressure direction and the side surface (SS) parallel to the sintering pressure direction of the samples sintered with SPS using different temperatures. All samples showed the diffraction peak of the hexagonal structure in the XRD patterns (Fig. 5a–c). In all the samples, the diffraction intensities of the (002) plane were higher than the diffraction intensities of the (100) plane on the TS surfaces, but were lower on the SS surfaces. Because of sintering with SPS, it was observed that the grain tendency oriented of hBN formation parallel to the pressure direction was along the c-axis. To determine the effects of the sintering temperature on the orientation of the samples, identified using X-ray diffraction, orientation preference index (IOP) values were calculated according to the following formula (Eq. 3) [3,18,22,23];

$$\mathrm{IOP} = \begin{cases} \dfrac{(I_{100}/I_{002})TS}{(I'_{100}/I'_{002})SS}, (I_{100}/I_{002})TS > (I'_{100}/I'_{002})SS \\ -\dfrac{(I'_{100}/I'_{002})SS}{(I_{100}/I_{002})TS}, (I_{100}/I_{002})TS < (I'_{100}/I'_{002})SS \end{cases} \quad (3)$$

where I_{hkl} and I'_{hkl} are the diffraction intensities of the peaks for to the top and side surfaces, respectively. If IOP = ±1, the (100) and (002) planes have the same diffraction intensity and that it consists of randomly oriented hBN grains. If IOP >1, the c-axis of hBN grains orients perpendicular to the sintering pressure direction. If IOP <−1, this indicates that hBN grains orient parallel to the sintering pressure direction.

Fig. 5 d gives IOP and the densities of the samples sintered at different temperatures. The IOP values for the hBN-1500, hBN-1700, and hBN-1900 samples resulted in negative values of −13184.2, −19925.5, and −2993.6, respectively. In this study, the IOP values showed negative values with a high absolute value, indicating a better texture degree, which is parallel to the pressure direction of the hBN grains [5,17,22,23]. Compared to textured ceramics prepared under conventional pressure conditions [16,18,23,53,54], this study shows that highly oriented hBN textured ceramics can be synthesized in situ with SPS. The literature reports that hBN has a microstructure in which the grains sintered with SPS are oriented parallel to the pressing direction, while the microstructures of the grains sintered by hot press processes are randomly aligned [29]. The hBN-1700 sample has the highest orientation, with an IOP value of −19925.5. This value is higher than for hBN synthesized product using hot press without the addition of sintering [17] and with the addition of Mullite [5,16], MAS (MgO powder, Al_2O_3 powder and fused silica powder) [18,19], YAG (reaction between Y_2O_3 and Al_2O_3) [22,23], metallic copper [3,20] sintering. This result

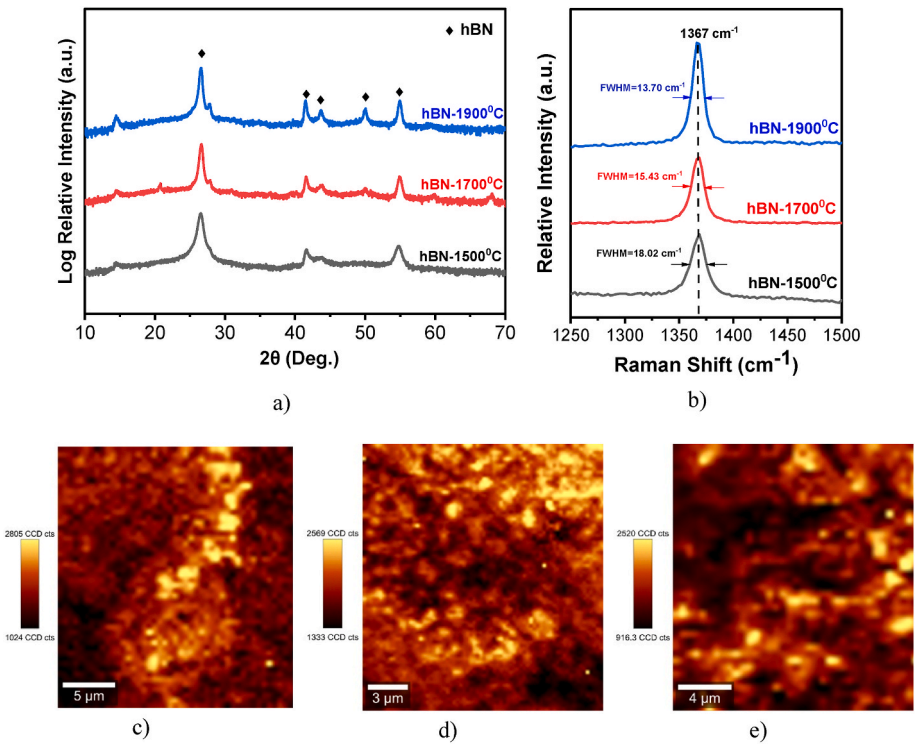

Fig. 4. Characterization of sintered using SPS the hBN-1500, hBN-1700 and hBN-1900 samples a) XRD patterns b) Raman spectrums, and Raman map of the peak for hBN samples (image used 20 μm × 20 μm square image at band around 1367 cm^{-1}) c) the hBN-1500, d) the hBN-1700, e) the hBN-1900.

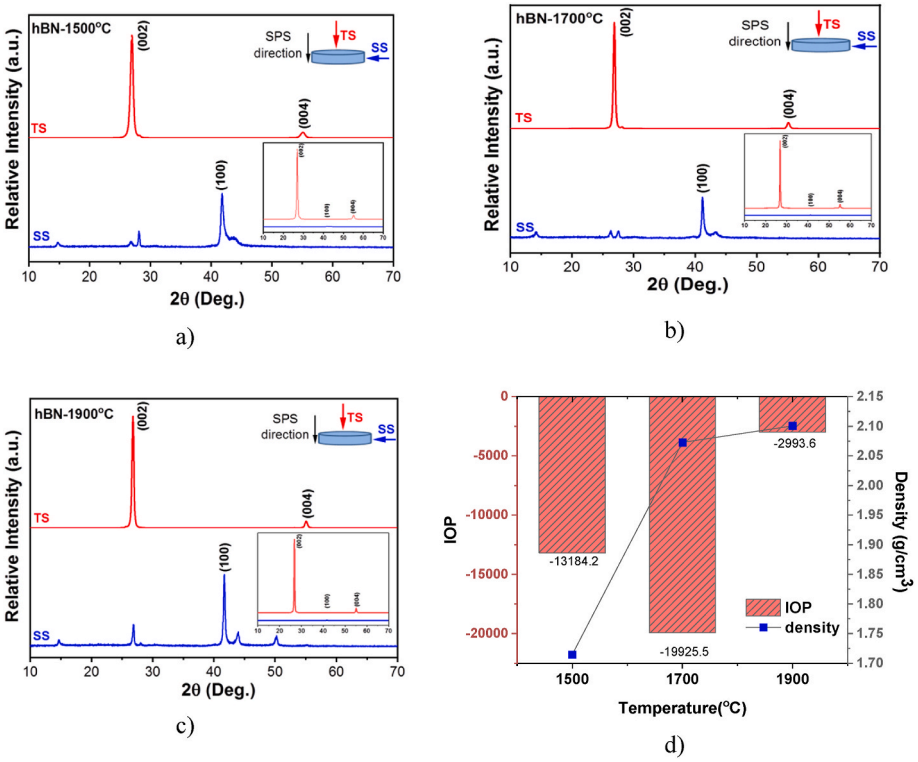

Fig. 5. XRD patterns of the top surface and side surface of samples sintered at different temperatures a) the hBN-1500, b) the hBN-1700 and c) the hBN-1900 d) the relationship of IOP values and density with sintered temperatures.

shows that in situ hBN synthesized with SPS has a higher texture degree orientation in the direction parallel to the pressing direction. When the temperature was increased to 1900 °C, the c-axis parallel orientation decreased with the increase in density, and as a result, IOP decreased to −2993.6. In samples sintered at higher temperatures, the (002) planes were not oriented to each other and became increasingly disordered. For the hBN sintered at higher temperatures, there is a random structure in both directions, which is compatible with the literature [17,18,27]. The

results indicate that high sintering temperature will decrease orientation in the direction parallel to the pressing direction. According to the results of true density measurements with a pycnometer, the density values increased with high temperature (Fig. 5d). The relative density was calculated as 75.53, 91.31 and 92.55 % at 1500 °C, 1700 °C and 1900 °C, respectively (which is the theoretical density of hBN 2.27 gcm^{-3}). At high temperatures with densification, grain growth increases significantly as a result of the increase in the diffusion rate of atoms. Depending on the grain growth in the sample sintered at 1900 °C, the orientation of the hBN grains decreased due to distortion caused by the collision of the edges of the grains [18].

Additionally, to evaluate preferential hBN grain orientation, the Lotgering factor was employed to calculate the orientation factor (F), which gauges the degree of preferential orientation of hBN grains aligned with the SPS pressing direction. The F value was extracted by analysis of the XRD patterns, presented in Fig. 5 a-c, the intensity of the diffraction peak was calculated according to the following formula (Eq. 4) [55–58];

$$F = \frac{P - P_0}{1 - P_0} \tag{4}$$

$$P_0 = \frac{\sum I_0(00l)}{\sum I_0(hkl)}, \text{and } P = \frac{\sum I(00l)}{\sum I(hkl)}$$

where I_0 and I represent the XRD peak intensities of surfaces parallel (SS) and perpendicular (TS) to the sintering pressure direction of the samples, respectively. The value of the F factor: F = 1 corresponds to a completely oriented sample, while F = 0 is attributed to the characteristic of a completely random grain orientation (non-oriented) sample. The F value was estimated at different temperatures. The F values of hBN-1500, hBN-1700 and hBN-1900 samples resulted in a value close to 1 as 0.996, 0.997 and 0.993, respectively. The orientation factor was determined as a characteristic of highly textured material for all samples. According to the results, the orientation of hBN parallel to the pressing direction increased with the SPS.

Fig. 6 shows SEM images of the fractured surfaces of the sintered samples. Fig. 6 (a, d, g) exhibits SEM micrographs of the fractured surface perpendicular to the sintering pressure direction. The hBN grains were aligned in the same direction. The hBN plate particles were oriented parallel to the SPS pressing direction and enhanced the grain growth of hBN with increasing temperature. Fig. 6 (b, e, h) shows SEM micrographs of the fractured surface parallel to the sintering pressure direction. Especially, Fig. 6b and e showed that the fracture surfaces were perpendicular to the c-axis orientation of hBN grains, which showed the hBN plate to have texture structures. The analysis of SEM micrographs and IOP values reveals a discernible level of parallel orientation of (002) planes in both the top surface and side surface of these samples. Conversely, in the hBN-1900 sample sintered at 1900 °C compared to other samples, the hBN grains were slightly oriented, although there was a randomly aligned (Fig. 6h). Furthermore, the hBN grain size was increased, showing that high-temperature enhanced the grain growth. This is consistent with the size of the crystallites, as

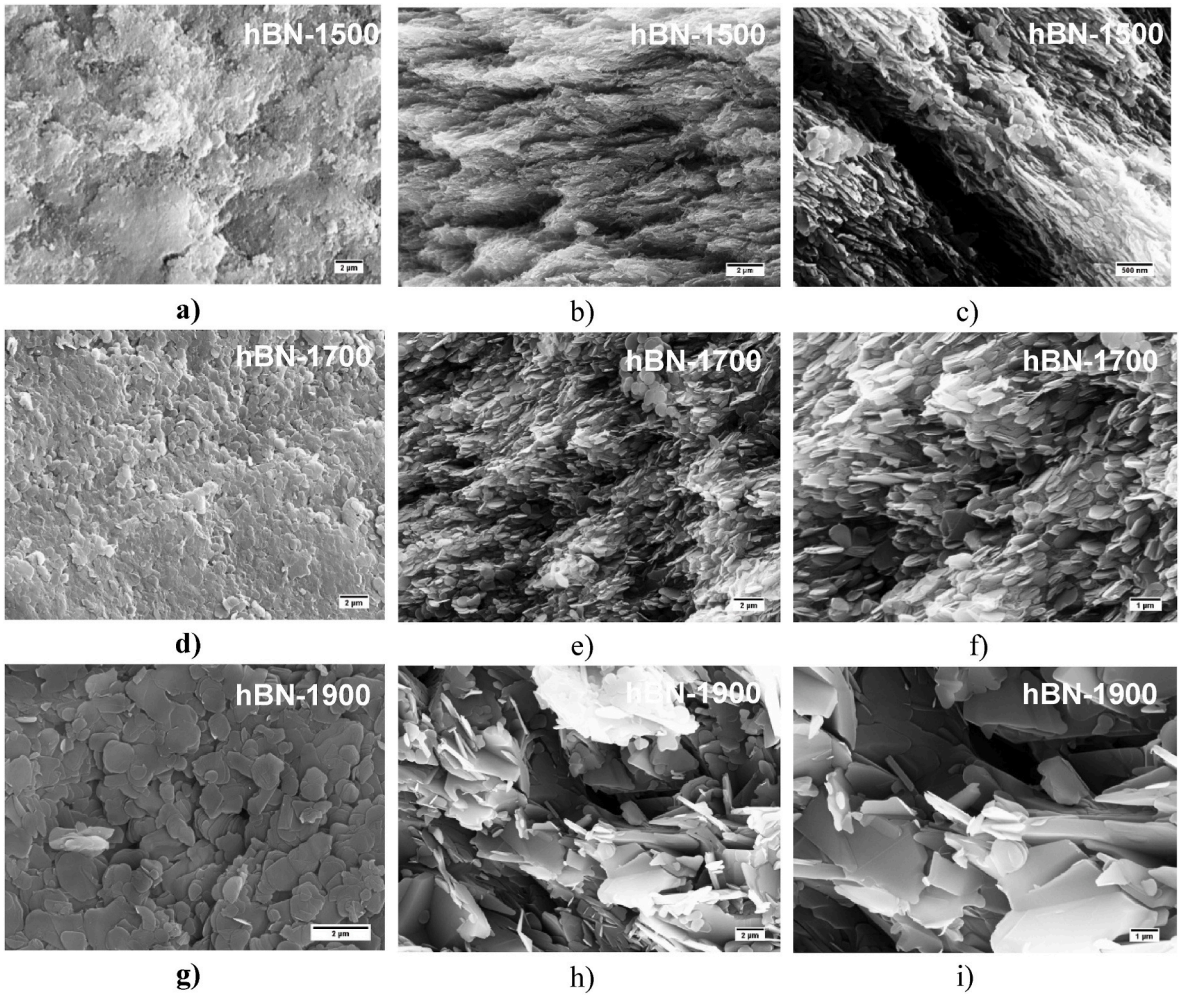

Fig. 6. (A–i) SEM images of the fractured surfaces of samples sintered at different temperatures (a, d, g) perpendicular, (b, e, h) parallel to the SPS sintering pressure direction and (c, f, i) high magnification image.

calculated using the Debye-Scherrer method. This large increase in grain size at high temperatures corresponds to a change in orientation factor, which may be responsible for the formation of the semi-isotropic structure [27]. The findings indicate that the orientation of the hBN grains will decrease with increasing temperature [18]. The results are under the corresponding lower IOP values at 1900 °C. Mateti et al. [27] stated that the anisotropic structure of hBN crystals is usually formed in hot pressing and SPS processes under high compression pressure in the intermediate temperature range (<1800 °C). They reported that during sintering at a high temperature of 1800–2300 °C, as a result of the increase of high current pulses, the electric field between the electrodes parallel to the coaxial direction and lifts the charged nanosheets, while the compression force presses the nanosheets down. For this reason, they stated that the electric force is balanced with the compression force so that larger (002) plates are formed in all directions. This approach explains the reduction in orientation of hBN grains at 1900 °C. When Fig. 6 (c, f, i) with high magnification is examined, samples have nano-size hBN grains at 1500 and 1700 °C, while it has nano-size and micron-size hBN grains at 1900 °C.

Fig. 7 shows AFM images of the topography of the native material obtained with the Gwyddion program from Fig. 6 a,d,g SEM images. These images provide information about the surface roughness perpendicular to the pressing direction. The surfaces of the samples were untreated and the surface roughness values were similar across all samples. The observation revealed that hBN orientation aligned parallel to the pressing direction in every sample.

3.3. Thermal conductivity

In the literature, the thermal conductivity of hBN at room temperature along the c-axis and a-axis was calculated as 4.1 and 537 $Wm^{-1}K^{-1}$, respectively [6]. Therefore, it is important to determine the thermal conductivity of the textured hBN. The thermal diffusivity of the samples was determined using a Laser Flash spectrometer at 25–400 °C range in top surface. The thickness of the samples is about 2 mm and the side surface is too small to be measured, so measurement could not be made with laser flash spectrometry. The thermal conductivity (k) was calculated from the following formula (Eq. 5);

$$k = \varphi\rho C_p \quad (5)$$

Where φ is thermal diffusivity, and ρ is the density of the sample, respectively. Cp is the specific heat capacity obtained depending on the temperature with the Shomate Equation [59]. The following formula (Eq. 6);

$$C_p^{\circ} = A + Bxt + Cxt^2 + Dxt^3 + E/t^2 \quad (6)$$

Where C_p° is the specific heat capacity, t is the temperature (K)/1000 and A-E are the coefficients for hBN used in the range 298–1100 ^{0}K.

Fig. 8 shows the thermal diffusivity and the calculated thermal conductivity values. Fig. 8b shows the increase in conductivity for samples sintered at increasing temperatures. The highest thermal conductivity values are 2.21 $Wm^{-1}K^{-1}$, 3.3 $Wm^{-1}K^{-1}$ and 8.86 $Wm^{-1}K^{-1}$ at 1500 °C, 1700 °C and 1900 °C, respectively. In addition, the conductivity increases up to 300 °C as the measurement temperature increases and then decreases. Heat is transferred by the movement of phonons in compounds like hBN. When photons are blocked by interphases or structural faults, it reduces the phonon mean free path as it causes phonon scattering, and thermal conductivity decreases [60]. At higher temperatures, a decreasing trend in the thermal conductivity with temperature which is expected because of the increase in phonon-phonon scattering. It has been reported that phonon lifetime decreases as the temperature increases [61]. Because of this factor, as seen in Fig. 8, there was a decrease in thermal conductivity observed during high-temperature measurements. Due to the smaller grain size in the hBN-1500 and hBN-1700 samples, more grain boundaries are formed, resulting in higher defect concentrations. This reduces free paths of the phonon because of strong phonon scattering at the interfaces and therefore reduces the thermal conductivity [61]. Moreover, the relative density for the hBN-1500 sample was calculated as 75.53%, while the relative density was over 90% for the other samples. The observed low density indicates an increase in porosity within the structure. Additionally, the thermal conductivity of air (0.026 $Wm^{-1}K^{-1}$) is significantly lower than hBN, thus contributing to the decrease in thermal conductivity [18]. Effective phonon scattering by pores is another factor that reduces thermal conductivity [62]. The reason there is no decrease in thermal conductivity measurement with

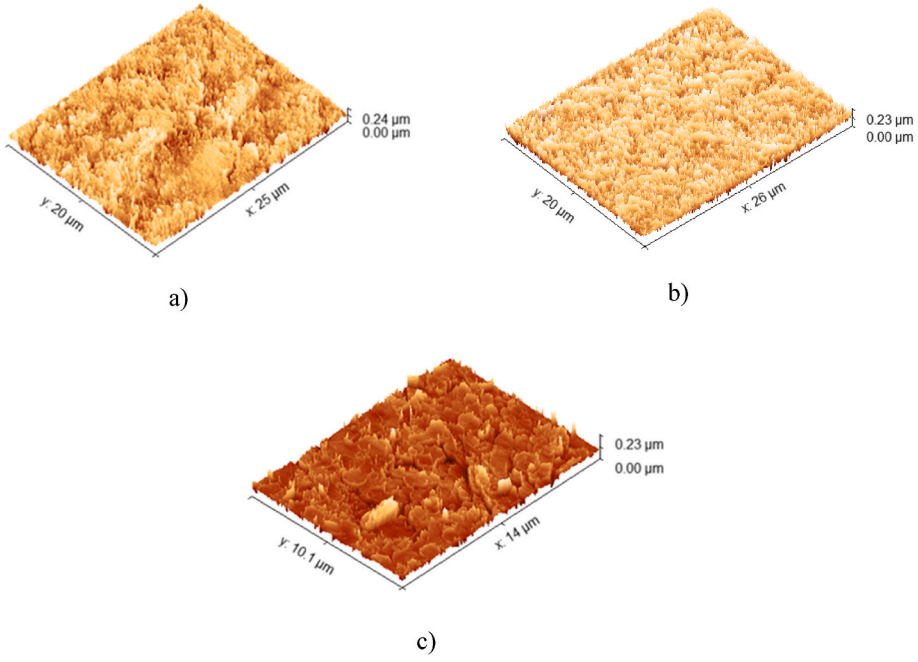

Fig. 7. AFM images of the topography perpendicular to the SPS sintering pressure direction at different temperatures a) the hBN-1500, b) the hBN-1700 and c) the hBN-1900 samples.

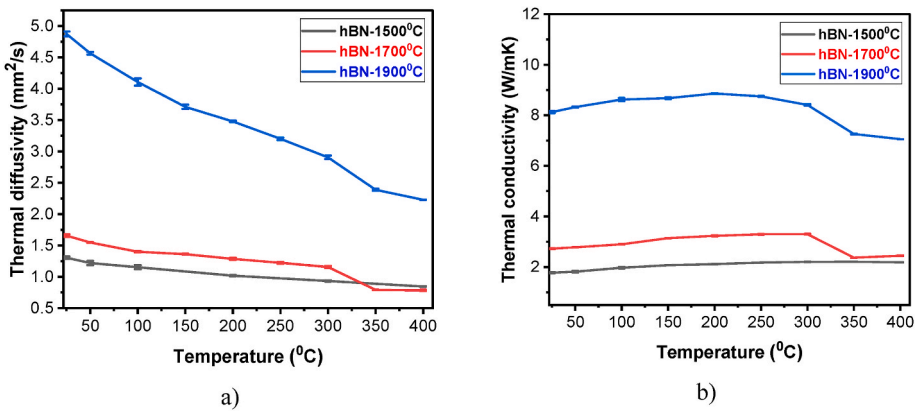

Fig. 8. Effect of sintered temperature on (a) thermal diffusivity and (b) thermal conductivity parallel (to surface) to the SPS sintering pressure direction.

increasing temperature in this sample can be attributed to the fact that phonon scattering is already significantly high at all temperatures, because of the porous structure and small grain size.

After sintering, the hBN (002) basal plane is aligned in the parallel to pressing directions. It has a high thermal conductivity in the perpendicular direction but in the parallel direction is low due to the cross-plane conductivity reasoned by weak van der Waals interactions between the (002) base planes. Mateti et al. [27] measured the thermal conductivity as approximately 14.3 $Wm^{-1}K^{-1}$ in the sample produced by SPS at 2200 °C from hBN powders with a diameter of several micrometers in this direction. Furthermore, the better crystal structures and larger BN crystallite sizes have higher thermal conductivity. It is reported that an SPS temperature of 2000 °C or higher causes drastically altered the microstructures, leading to a quasi-isotropic thermal conductivity. The (002) planes are not oriented towards each other under compression pressure in samples sintered at high temperatures and more irregular pellets are formed. In this study, the highest thermal conductivity was measured as approximately 8.86 $Wm^{-1}K^{-1}$ in the sample sintered at 1900 °C. The thermal conductivity of the sample sintered at 1900 °C is higher than the samples sintered at 1500 °C and 1700 °C because of the larger hBN crystallite size (23.82 nm) and less orientation (IOP value −2993.6). A low IOP value indicates an increased random orientation in both directions. The IOP values for the hBN-1500 and hBN-1700 samples (−13184.2 and −19925.5, respectively) show that have a typical anisotropic structure, contributing to the low cross-plane conductivity measured. As a result of this anisotropic structure, the highest thermal conductivity values for the hBN-1500 and hBN-1700 samples perpendicular to the pressing direction are 2.21 $Wm^{-1}K^{-1}$ and 3.3 $Wm^{-1}K^{-1}$, respectively. These results are much lower than studies in the literature [18,27]. Therefore, these two samples (hBN-1500 and hBN-1700) with high IOP values, examining the thermal properties in the side surface direction, may be interesting for later studies.

Niu et al. [18] showed IOP value of −16.7 at 0.5 μm hBN particle size in hot-press sintered hBN-MAS composite ceramic at 1800 °C. They reported that, with increased raw hBN particle sizes from 5.0 μm to 11.0 μm, IOP values increased from −717.4 to −5413.6. This shows that the texture degree increases significantly with increasing raw hBN particle size. As a result, the thermal conductivity of the top surface decreased while the side surface increased [19]. In this study, in which hBN synthesis was performed in situ with SPS, the thermal conductivity on the top surface increased with increasing hBN particle size. Especially for hBN synthesized in situ with SPS at low temperatures, low thermal conductivity in the top surface direction indicates excellent thermal protection in this direction. The hBN is quite stable in an oxygen atmosphere up to a heating temperature of 860 °C and retains its atomic structure. At higher temperatures, it undergoes oxidation with the formation of B_2O_3 [62,63]. Additionally, highly oriented hBN nanosheets have been shown in studies to have better thermal stability compared to randomly oriented sheets [64]. A study showed that when hBN was treated with molecular oxygen at low temperatures, the O_2 molecule did not dissociate and accumulated state to perfect lattice by binding to the surface of hBN as peroxide or superoxide at low concentrations, proving its high chemical stability [62]. The hBN plates will act as barriers to heat conduction along the pressure direction when the texture features are strong. In addition to this feature, its thermal stability enables the creation of products that align with the requirements and specifications of various industries.

4. Conclusion

The precursor formation of tBN started at 850 °C and hBN was obtained at all sintering temperatures with SPS. The XRD patterns and Raman results show that high temperature could significantly improve the crystalline of hBN. The synthesis resulted in a homogeneous structure and multi-layered hBN. Negative IOP values with a high absolute value compared to textured ceramics prepared under conventional pressure conditions, this study shows that highly oriented hBN textured ceramics can be synthesized in situ by SPS. The highest orientation was obtained with an IOP value of −19925.5 at 1700 °C. hBN plate particles were oriented parallel to the SPS pressing direction and enhanced the grain growth of hBN with increasing temperature. The highest thermal conductivity was measured 8.86 $Wm^{-1}K^{-1}$ in the sample sintered at 1900 °C. The low thermal conductivity obtained in the top surface direction at low temperatures (1500 °C and 1700 °C), indicates excellent thermal protection in this direction for hBN synthesized in situ with SPS. When hBN plates have strong texture features, they function as an effective thermal barrier and enable the development of diverse industrial applications.

CRediT authorship contribution statement

Zuhal Yılmaz: Conceptualization, Data curation, Formal analysis, Funding acquisition, Investigation, Methodology, Project administration, Resources, Supervision, Writing – original draft, Writing – review & editing. **Nuran Ay:** Conceptualization, Resources, Funding acquisition, Methodology, Supervision, Writing – review & editing.

Declaration of competing interest

The authors declare that they have no known competing financial interests or personal relationships that could have appeared to influence the work reported in this paper.

Data availability

No data was used for the research described in the article.

Acknowledgments

The authors would like to acknowledge the MIDAS (Micro/nano Devices and Systems) laboratory, SAM (Ceramics Research Center), Prof. Esin APAYDIN VAROL and Asst. Prof. Murat KILIÇ from the Department of Chemical Engineering at Eskişehir Technical University.

References

[1] X. Shi, S. Wang, H. Yang, X. Duan, X. Dong, Fabrication and characterization of hexagonal boron nitride powder by spray drying and calcining-nitriding technology, J. Solid State Chem. 181 (9) (Sep. 2008) 2274–2278, https://doi.org/10.1016/J.JSSC.2008.05.029.
[2] X.F. Jiang, et al., Recent progress on fabrications and applications of boron nitride nanomaterials: a review, J. Mater. Sci. Technol. 31 (6) (2015) 589, https://doi.org/10.1016/J.JMST.2014.12.008. Jun.
[3] M. Hubáček, M. Ueki, Effect of the orientation of boron nitride grains on the physical properties of hot-pressed ceramics, J. Am. Ceram. Soc. 82 (1) (1999) 156–160, https://doi.org/10.1111/j.1151-2916.1999.tb01735.x.
[4] J. Duan, R. Xue, Y. Xu, C. Sun, Low temperature synthesis of h-BN nanoflakes, Mater. Lett. 62 (19) (Jul. 2008) 3355–3357, https://doi.org/10.1016/J.MATLET.2008.03.007.
[5] X. Duan, et al., Materials Science & Engineering A Anisotropic mechanical properties and fracture mechanisms of textured h-BN composite ceramics, Mater. Sci. Eng. A 607 (2014) 38–43, https://doi.org/10.1016/j.msea.2014.03.132.
[6] P. Jiang, X. Qian, R. Yang, L. Lindsay, Anisotropic thermal transport in bulk hexagonal boron nitride, Phys. Rev. Mater. 2 (6) (2018), https://doi.org/10.1103/PhysRevMaterials.2.064005.
[7] T.E. Oconnor, Synthesis of boron nitride, J. Am. Chem. Soc. 84 (9) (1962) 1753–1754, https://doi.org/10.1021/JA00868A065.
[8] J. Thomas, N.E. Weston, T.E. O'connor, Turbostratic 1 boron nitride, thermal transformation to ordered-layer-lattice boron nitride, J. Am. Chem. Soc. 84 (24) (1962) 4619–4622, https://doi.org/10.1021/JA00883A001/ASSET/JA00883A001.FP.PNG_V03.
[9] T.E. O'Connor, Process for the Production of Boron Nitride, 1966.
[10] D.H.A. Besisa, M.A.A. Hagras, E.M.M. Ewais, Y.M.Z. Ahmed, Z.I. Zaki, A. Ahmed, Low temperature synthesis of nano-crystalline h-boron nitride from boric acid/urea precursors, J. Ceram. Process. Res. 17 (12) (2016) 1219–1225.
[11] M. Ueki, U. Professional, Role of Boron Oxide in Growth of Boron Nitride Grains, March, 2018.
[12] M. Hubáček, M. Ueki, T. Sato, V. Brozek, High-temperature behaviour of hexagonal boron nitride, Thermochim. Acta 282/283 (1996) 359–367.
[13] M. Hubáček, M. Ueki, Chemical reactions in hexagonal boron nitride system, J. Solid State Chem. 123 (2) (1996) 215–222, https://doi.org/10.1006/jssc.1996.0171.
[14] T. Hagio, K. Kobayashi, H. Yoshida, H. Yasunaga, H. Nishikawa, Sintering of the mechanochemically activated powders of hexagonal boron nitride, J. Am. Ceram. Soc. 72 (8) (1989) 1482–1484, https://doi.org/10.1111/j.1151-2916.1989.tb07682.x.
[15] T. Hagio, K. Nonaka, T. Sato, Microstructural development with crystallization of hexagonal boron nitride, J. Mater. Sci. Lett. 16 (10) (1997) 795–798, https://doi.org/10.1023/A:1018518222594/METRICS.
[16] X. Duan, et al., Effect of sintering pressure on the texture of hot-press sintered hexagonal boron nitride composite ceramics, Scripta Mater. 68 (2) (2013) 104–107, https://doi.org/10.1016/j.scriptamat.2012.09.012.
[17] J.X. Xue, J.X. Liu, B.H. Xie, G.J. Zhang, Pressure-induced preferential grain growth, texture development and anisotropic properties of hot pressed hexagonal boron nitride ceramics, Scripta Mater. 65 (11) (2011) 966–969, https://doi.org/10.1016/j.scriptamat.2011.08.025.
[18] B. Niu, et al., Effects of sintering temperature on the microstructure and properties of h-BN ceramics with MAS as liquid sintering aid, Ceram. Int. 46 (1) (2020) 1076–1082, https://doi.org/10.1016/j.ceramint.2019.09.074.
[19] B. Niu, D. Cai, Z. Yang, X. Duan, Y. Sun, H. Li, Journal of the European Ceramic Society Anisotropies in structure and properties of hot-press sintered h -BN-MAS composite ceramics : effects of raw h -BN particle size, J. Eur. Ceram. Soc. 39 (2–3) (2019) 539–546, https://doi.org/10.1016/j.jeurceramsoc.2018.08.043.
[20] M. Hubáček, T. Sato, M. Ueki, Copper-boron nitride interaction in hot-pressed ceramics, J. Mater. Res. 12 (1) (1997) 113–118, https://doi.org/10.1557/JMR.1997.0018.
[21] T. Kusunose, T. Sekino, Thermal conductivity of hot-pressed hexagonal boron nitride, Scripta Mater. 124 (Nov. 2016) 138–141, https://doi.org/10.1016/j.scriptamat.2016.07.011.
[22] Z. Tian, Y. Wang, Z. Zhang, X. Duan, D. Jia, S. Wu, Preparation of highly oriented h-BN based textured ceramics via grain rearrangement under DLP printing and low-pressure sintering, Mater. Lett. 268 (2020) 127584, https://doi.org/10.1016/j.matlet.2020.127584.
[23] Z. Zhang, et al., Texture and anisotropy of hot-pressed h-BN matrix composite ceramics with in situ formed YAG, J. Adv. Ceram. 11 (4) (2022) 532–544, https://doi.org/10.1007/s40145-021-0553-3.
[24] M. Tokita, Mechanism of Spark Plasma Sınterıng. Japan : Sumltomo Coal Mlmng Company, Ltd.
[25] Z.H. Zhang, Z.F. Liu, J.F. Lu, X.B. Shen, F.C. Wang, Y.D. Wang, The sintering mechanism in spark plasma sintering – proof of the occurrence of spark discharge, Scripta Mater. 81 (Jun. 2014) 56–59, https://doi.org/10.1016/J.SCRIPTAMAT.2014.03.011. Complete.
[26] J.-L. Huang, P. K, Effect of nano-TiN on mechanical behavior of Si3N4 based nanocomposites by spark plasma sintering (SPS), in: Nanocomposites - New Trends and Developments, IntechOpen, 2012.
[27] S. Mateti, et al., Bulk hexagonal boron nitride with a quasi-isotropic thermal conductivity, Adv. Funct. Mater. 28 (2018) 28, https://doi.org/10.1002/adfm.201707556.
[28] D.W. Ni, G.J. Zhang, Y.M. Kan, Y. Sakka, Textured h-BN ceramics prepared by slip casting, J. Am. Ceram. Soc. 94 (5) (2011) 1397–1404, https://doi.org/10.1111/j.1551-2916.2010.04273.x.
[29] T.F. Almeida, M.P. Gonçalves, R.H.G.A. Kiminami, Microstructure and dielectric properties of hexagonal boron nitride prepared by hot pressing (uniaxial and isostatic) and by spark plasma sintering, 10.1080/17436753.2019.1689704 119 (1) (Jan. 2019) 41–48, https://doi.org/10.1080/17436753.2019.1689704.
[30] M. Ehsani, M. Zakeri, M. Razavi, The effect of boron oxide on the physical and mechanical properties of nanostructured boron nitride by spark plasma sintering, J. Alloys Compd. 780 (Apr. 2019) 570–573, https://doi.org/10.1016/J.JALLCOM.2018.11.341.
[31] C. Steinborn, et al., Correlation between microstructure and electrical resistivity of hexagonal boron nitride ceramics, J. Eur. Ceram. Soc. 33 (6) (2013) 1225–1235, https://doi.org/10.1016/j.jeurceramsoc.2012.11.024.
[32] Y. Li, et al., Advanced synthesis of highly crystallized hexagonal boron nitride by coupling polymer-derived ceramics and spark plasma sintering processes - influence of the crystallization promoter and sintering temperature, Nanotechnology 30 (3) (2019), https://doi.org/10.1088/1361-6528/aaebb4.
[33] H. Eslami-shahed, K. Nekouee, N. Ehsani, Synthesis of h-BN through spark plasma sintering with urea and boric acid as the starting materials, Diam. Relat. Mater. 124 (2022) 108915, https://doi.org/10.1016/j.diamond.2022.108915. December 2021.
[34] Z. Yılmaz, U. Savacı, S. Turan, N. Ay, The effect of in-situ formed layered hBN on the machinability and mechanical properties of SPS sintered SiC, Ceram. Int. 48 (1) (Jan. 2022) 1047–1056, https://doi.org/10.1016/J.CERAMINT.2021.09.190.
[35] J. Qu, Q. Li, C. Luo, J. Cheng, X. Hou, Characterization of flake boron nitride prepared from the low temperature combustion synthesized precursor and its application for dye adsorption, Coatings 8 (2018) 6, https://doi.org/10.3390/coatings8060214.
[36] Z. Yılmaz, N. Ay, Production parameters affecting the synthesis and properties of hBN-SiC composites, J. Australas. Ceram. Soc. 56 (1) (Mar. 2020) 99–108, https://doi.org/10.1007/S41779-019-00398-4.
[37] U. Holzwarth, N. Gibson, The Scherrer equation versus the 'Debye-Scherrer equation, 2011 69, Nat. Nanotechnol. 6 (9) (Aug. 2011) 534, https://doi.org/10.1038/nnano.2011.145, 534.
[38] L. Durai, P. Yadav, H. Pant, V.V.S.S. Srikanth, S. Badhulika, Label-free wide range electrochemical detection of β-carotene using solid state assisted synthesis of hexagonal boron nitride nanosheets, New J. Chem. 44 (37) (2020) 15919–15927, https://doi.org/10.1039/d0nj03170d.
[39] M. Oz, N.K. Saritekin, C. Bozkurt, E. Budak, G. Yildirim, Effect of Li2CO3 on formation temperature of hBN by modified O'Connor model, Cryst. Res. Technol. 51 (12) (2016) 708–717, https://doi.org/10.1002/crat.201600138.
[40] X. Chen, et al., Effect of employing chromium as a buffer layer on the crystallinity of hexagonal boron nitride films grown by LPCVD, J. Mater. Sci. Mater. Electron. 32 (10) (2021) 13961–13971, https://doi.org/10.1007/s10854-021-05972-w.
[41] S. Liu, et al., Large-Scale growth of high-quality hexagonal boron nitride crystals at atmospheric pressure from an Fe-Cr flux, Cryst. Growth Des. 17 (9) (2017) 4932–4935, https://doi.org/10.1021/acs.cgd.7b00871.
[42] J. Liu, R.G. Kutty, Z. Liu, Controlled synthesis of atomically layered hexagonal boron nitride via chemical vapor deposition, Molecules 21 (2016) 12, https://doi.org/10.3390/molecules21121636.
[43] A. Vokhmintsev, I. Weinstein, D. Zamyatin, Electron-phonon interactions in subband excited photoluminescence of hexagonal boron nitride, J. Lumin. 208 (2019) 363–370, https://doi.org/10.1016/j.jlumin.2018.12.036.
[44] B. Singh, et al., Nanostructured boron nitride with high water dispersibility for boron neutron capture therapy, Sci. Rep. 6 (2016), https://doi.org/10.1038/srep35535. October.
[45] R.J. Nemanich, S.A. Solin, R.M. Martin, Light scattering study of boron nitride microcrystals, Phys. Rev. B 23 (12) (1981) 6348–6356, https://doi.org/10.1103/PhysRevB.23.6348.
[46] M. Franck, J. Dabrowski, M.A. Schubert, C. Wenger, M. Lukosius, Towards the growth of hexagonal boron nitride on Ge(001)/Si substrates by chemical vapor deposition, Nanomaterials 12 (2022) 19, https://doi.org/10.3390/nano12193260.
[47] R. Singhal, E. Echeverria, D.N. McIlroy, R.N. Singh, Synthesis of hexagonal boron nitride films on silicon and sapphire substrates by low-pressure chemical vapor deposition, Thin Solid Films 733 (2021) 138812, https://doi.org/10.1016/j.tsf.2021.138812. July.
[48] X. Chen, et al., Growth of hexagonal boron nitride films on silicon substrates by low-pressure chemical vapor deposition, J. Mater. Sci. Mater. Electron. 32 (3) (Feb. 2021) 3713–3719, https://doi.org/10.1007/S10854-020-05116-6/FIGURES/5.

[49] K. Krishnamoorthy, S.-J. Kim, K. Krishnamoorthy, S.-J. Kim, Raman spectroscopy and mapping analysis of low-dimensional nanostructured materials and systems, Recent Dev. At. Force Microsc. Raman Spectrosc. Mater. Charact., Sep. (2021), https://doi.org/10.5772/INTECHOPEN.99775.
[50] V. Shautsova, A.M. Gilbertson, N.C.G. Black, S.A. Maier, L.F. Cohen, Hexagonal Boron Nitride assisted transfer and encapsulation of large area CVD graphene, Sci. Rep. 6 (Jul) (2016), https://doi.org/10.1038/SREP30210.
[51] C.R. Woods, et al., Commensurate-incommensurate transition in graphene on hexagonal boron nitride, Nat. Phys. 10 (6) (2014) 451–456, https://doi.org/10.1038/nphys2954.
[52] M.H. Khan, et al., Few-atomic-layered hexagonal boron nitride: CVD growth, characterization, and applications, Mater. Today 20 (10) (2017) 611–628, https://doi.org/10.1016/j.mattod.2017.04.027.
[53] N. Sun, J. Sun, X. Zeng, P. Chen, J. Qian, R. Xia, U. Professional, Preparation and anisotropic properties of textured structural ceramics: a review. Scripta M, Scripta Mater. 3 (1) (2020) 38–43, https://doi.org/10.1021/acs.nanolett.9b05268. Jul. 2020.
[54] L. Sun, J. Sun, L. Chen, P. Niu, X. Yang, Y. Guo, Preparation and characterization of chitosan film incorporated with thinned young apple polyphenols as an active packaging material, Carbohydr. Polym. 163 (2017) 81–91, https://doi.org/10.1016/j.carbpol.2017.01.016.
[55] M. Yaprintsev, A. Vasil'ev, O. Ivanov, Thermoelectric properties of the textured Bi1.9Gd0.1Te3 compounds spark-plasma-sintered at various temperatures, J. Eur. Ceram. Soc. 40 (3) (Mar. 2020) 742–750, https://doi.org/10.1016/J.JEURCERAMSOC.2019.11.028.
[56] O. Ivanov, M. Yaprintsev, A. Vasil'ev, Comparative analysis of the thermoelectric properties of the non-textured and textured Bi1.9Gd0.1Te3 compounds, J. Solid State Chem. 290 (Oct. 2020) 121559, https://doi.org/10.1016/J.JSSC.2020.121559.
[57] T. Kimura, T. Takahashi, T. Tani, Y. Saito, Crystallographic texture development in bismuth sodium titanate prepared by reactive-templated grain growth method, J. Am. Ceram. Soc. 87 (8) (2004) 1424–1429, https://doi.org/10.1111/J.1551-2916.2004.01424.X.
[58] S. Takahashi, Y. Imai, A. Kan, Y. Hotta, H. Ogawa, Dielectric and thermal properties of isotactic polypropylene/hexagonal boron nitride composites for high-frequency applications, J. Alloys Compd. 615 (2014) 141–145, https://doi.org/10.1016/j.jallcom.2014.06.138.
[59] M.W. Chase Jr., NIST-JANAF themochemical tables, J. Phys. Chem. Ref. Data, Monograph 9 (1998) 1–1951 [Online]. Available: https://srd.nist.gov/JPCRD/jpcrdM9.pdf.
[60] I.N. Qader, M.S. Omar, The effects of pressure and size parameter on the lattice thermal conductivity in multilayer hexagonal boron nitride, Iran. J. Sci. Technol. Trans. A Sci. 46 (6) (2022) 1705–1718, https://doi.org/10.1007/s40995-022-01370-x.
[61] B. Mortazavi, L.F.C. Pereira, J.W. Jiang, T. Rabczuk, Modelling heat conduction in polycrystalline hexagonal boron-nitride films, Sci. Rep. 5 (1) (Aug. 2015) 1–11, https://doi.org/10.1038/srep13228, 2015 51.
[62] L.Y. Antipina, L.A. Varlamova, P.B. Sorokin, The temperature dependence of the hexagonal boron nitride oxidation resistance, insights from First−Principle computations, Nanomaterials 13 (2023) 6, https://doi.org/10.3390/nano13061041.
[63] H. Jin, et al., Functionalization of hexagonal boron nitride in large scale by a low-temperature oxidation route, Mater. Lett. 175 (2016) 244–247, https://doi.org/10.1016/j.matlet.2016.04.008.
[64] I.S. Merenkov, et al., Orientation-controlled, low-temperature plasma growth and applications of h-BN nanosheets, Nano Res. 12 (1) (Jan. 2019) 91–99, https://doi.org/10.1007/S12274-018-2185-7/METRICS.